NANO LETTERS

Letter

Cite This: Nano Lett. 2018, 18, 1264−1268

pubs.acs.org/NanoLett

Proximity-Induced Superconductivity and Quantum Interference in Topological Crystalline Insulator SnTe Thin-Film Devices

Robin Klett,[*,†] Joachim Schönle,[‡] Andreas Becker,[†] Denis Dyck,[†] Kiril Borisov,[∥] Karsten Rott,[†] Daniela Ramermann,[†] Björn Büker,[†] Jan Haskenhoff,[†] Jan Krieft,[†] Torsten Hübner,[†] Oliver Reimer,[†] Chandra Shekhar,[§] Jan-Michael Schmalhorst,[†] Andreas Hütten,[†] Claudia Felser,[§] Wolfgang Wernsdorfer,[‡,∥] and Günter Reiss[*,†]

[†]Center for Spinelectronic Materials & Devices, Physics Department, Bielefeld University, Universitätsstraße 25, 33615 Bielefeld, Germany

[‡]CNRS, Institut NEEL and Université Grenoble Alpes, 38000 Grenoble, France

[§]Max Planck Institute for Chemical Physics of Solids, 01187 Dresden, Germany

[∥]Physics Department, Karlsruhe Institute of Technology, Wolfgang-Gaede-Straße 1, 76131 Karlsruhe, Germany

Supporting Information

ABSTRACT: Topological crystalline insulators represent a new state of matter, in which the electronic transport is governed by mirror-symmetry protected Dirac surface states. Due to the helical spin-polarization of these surface states, the proximity of topological crystalline matter to a nearby superconductor is predicted to induce unconventional superconductivity and, thus, to host Majorana physics. We report on the preparation and characterization of Nb-based superconducting quantum interference devices patterned on top of topological crystalline insulator SnTe thin films. The SnTe films show weak anti-localization, and the weak links of the superconducting quantum interference devices (SQUID) exhibit fully gapped proximity-induced superconductivity. Both properties give a coinciding coherence length of 120 nm. The SQUID oscillations induced by a magnetic field show 2π periodicity, possibly dominated by the bulk conductivity.

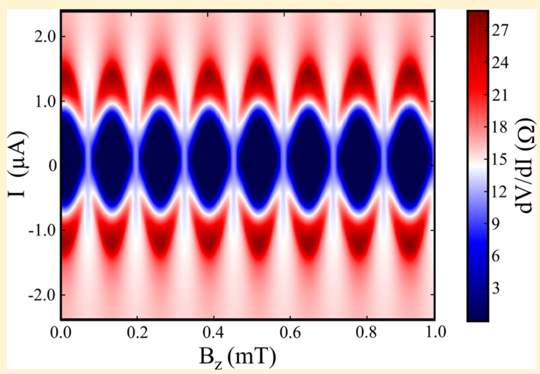

KEYWORDS: *Thin films, topological insulator, superconductivity, mesoscopic devices*

In the past several years, tremendous efforts have been made in investigating new topological states of matter, and it has been widely recognized that the family of topological materials is highly diversified and widespread.[1] One of its species is formed by topological crystalline insulators (TCI), in which topological protection is due to the symmetry of the crystal structures. The first predicted[2] and experimentally verified[3] class of TCI materials was found within the IV−VI semiconductors, with SnTe as a representative model material. SnTe crystallizes in rock-salt structure, and the symmetry responsible for its topological nature is the reflection symmetry with respect to the (110) mirror planes.[2,3] The appearance of unconventional boundary modes in such topologically nontrivial phases has been detected experimentally via several techniques,[4−6] manifesting themselves in linearly dispersing chiral topological surface states (TSS). One of the most-mesmerizing consequences of the TSS and nontrivial topology arises if the material itself undergoes a superconducting phase transition. In this case, theoretical models predict the occurrence of topological (mirror) superconductivity.[7] More specifically, the four Dirac cones in the TCI surface Brillouin zone give rise to host Majorana Fermion quartets.[8] For intrinsic superconducting TCI a couple of smoking gun experiments have been made in In-substituted $Sn_{1-x}In_xTe$,[9,10] which shows a superconducting phase transition at T_c = 3.5−4.7 K while maintaining its nontrivial band structure.[11] However, the issue of extrinsic (proximity-induced) superconductivity in undoped SnTe has not been tackled yet experimentally. In this case, the system can undergo a superconducting phase transition due to its proximity to a nearby conventional s-wave superconductor (SC).[12] Here, we report on the fabrication and characterization of SC−TCI hybrid microstructures. We patterned superconducting quantum interference devices (SQUIDs) made from Nb thin films on co-sputtered SnTe thin films such that bridges from SnTe form weak links between superconducting Nb wires. The resistance of the SnTe shows a weak anti-localization in its magnetic field response and the SnTe weak links become fully superconducting. We additionally studied the SQUID ring behavior in DC magnetic fields. Proximity

Received: November 17, 2017
Revised: January 14, 2018
Published: January 24, 2018

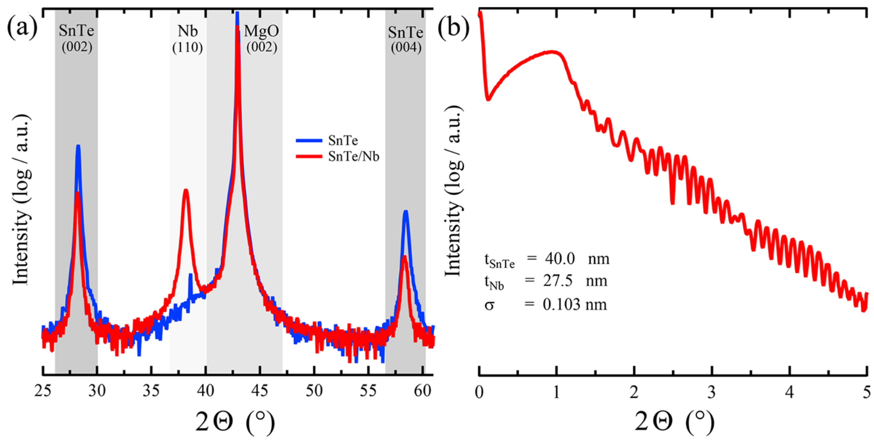

Figure 1. (a) XRD scans taken for a 50 nm and a 40 nm thick SnTe−27.5 nm Nb bilayer grown on a MgO (001) substrate. The SnTe films show a polycrystalline growth with a strong (001) texture. The subsequent Nb layer grows in (110) on top of the SnTe. (b) X-ray reflection measurements of the bilayer structures proof the flatness of the films with a roughness of only 0.1 nm and indicate low strain at the interface of both layers.

induced superconductivity on the TSS by s-wave SC is theoretically predicted to result in an anomalous 4π-periodic characteristic, which is superimposed on the conventional (2π-periodic) SQUID relation:

$$\phi_0 = \frac{h}{2e} = A_S \delta_B \tag{1}$$

where ϕ_0 is the magnetic flux quantum, A_S is the effective area of the SQUID, and δ_B is the oscillation period. A SQUID interference pattern hosting 4π-periodic physics would be an ultimate proof of topological superconductivity[13] and, hence, the presence of Majorana Fermions.

Sample Preparation. In this section, we describe the growth procedure of the TCI−SC hybrids and give a detailed description of the lithography and patterning process. First, thin films of SnTe are grown on MgO substrates at 150 °C via co-sputtering of Sn and Te. We chose insulating MgO (001) substrates due to their cubic crystal structure and their good lattice match to the SnTe lattice constant $a_{SnTe} = 0.63$ nm $\approx \sqrt{2}a_{MgO}$.[14] The base pressure of the sputter system is 5×10^{-10} mbar, the Ar-pressure is $p \approx 2.5 \times 10^{-3}$ mbar. As shown in Figure 1a, X-ray diffraction (XRD) in Θ−2Θ geometry clearly produces only the (002) and (004) diffraction peaks. Thus, under these conditions 40 nm SnTe thin films grow polycrystalline (PC) with strong (001) texture. In the next step the TCI thin films are coated with Nb, a well-characterized and established s-wave superconductor. The Nb is deposited without exposing the sample to ambient conditions to prevent TCI surface contamination and to allow a high transparency at the SnTe/Nb interface.[15,16] The nominally deposited 27.5 nm Nb films grow in (110) texture with low strain on top of the SnTe rock-salt lattice, which is confirmed with the XRD peak at 38.3° in Figure 1a. The X-ray reflection data presented in Figure 1b verify smooth film growth with a fitted roughness of $\sigma \approx 0.1$ nm. A low surface roughness has recently been identified as a crucial precondition for the presence of TSS in TCI films.[17,18] Further structural and surface analysis can be found in the Supporting Information. In particular, we performed high-resolution transmission electron microscopy imaging of cross-sections made by focused ion beam milling to further elucidate the microstructure of the MgO/SnTe/Nb film system. The results shown in the Figure S4 show a clean interface between the SnTe and the Nb and a well textured (001) columnar growth of the SnTe with a mean grain size of around 30 nm. Because Nb is known to be a chemically very active metal, the film quality (and the superconducting properties) often suffer from lithographic and etching processes during device patterning. We counter this issue by capping the TCI/SC hybrid with 2.5 nm of Ta and 5 nm of Ru as protection for subsequent fabrication steps. The SQUIDs are patterned with conventional e-beam lithography. After resist development, the film stacks are patterned by Ar-ion dry etching. Controlled via secondary ion mass spectroscopy, we stop the sample etching once the exposed Nb area is removed. In this way, patterned Nb defines the superconducting loop while the bottom SnTe film is intact. The patterned SQUIDs (exemplarily shown in Figure 2) have an effective area $A = 16$ μm^2 and the Nb lines have a width of $w = 200$ nm. The length L of the two Josephson junctions is varied between $L = 50$−200 nm. The samples are characterized electrically both by direct current measurements of the film resistance as well as by a current-biased lock-in technique for differential resistance dV/dI scans.

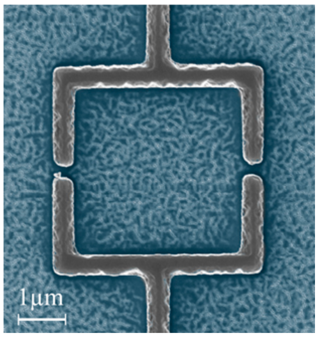

Figure 2. False-color SEM image of one of the fabricated SQUID samples. The Nb lines are highlighted in gray scale, while the SnTe film is pictured in dark blue. The nominally patterned inner area of the device is $A = 16$ μm^2, and the length of the weak links is $L_J = 120$ nm.

Results. *SnTe Thin-Film Magnetoresistance.* Before starting the characterization of the proximity induced superconductivity and the SQUID data, we investigate the transport properties of bare SnTe thin films using patterned Hall bar microstructures as schematically shown in the inset of Figure 3a. The determination of the Hall coefficient with Hall

DOI: 10.1021/acs.nanolett.7b04870
Nano Lett. 2018, 18, 1264−1268

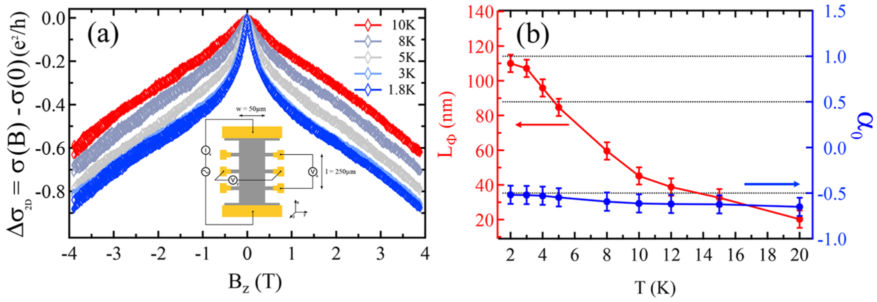

Figure 3. (a) Magneto-conductivity for several temperatures as a function of out-of-plane magnetic field B_z. The image in the inset shows the dimension of the micropatterned Hallbar devices. The data indicate weak anti-localization and, thus, give evidence for two-dimensional electronic transport. (b) Temperature dependence of the phase-coherence length L_Φ and the transport parameter α after fitting the low magnetic field (B_z < 0.5 T) conductivity within the HLN formalism.

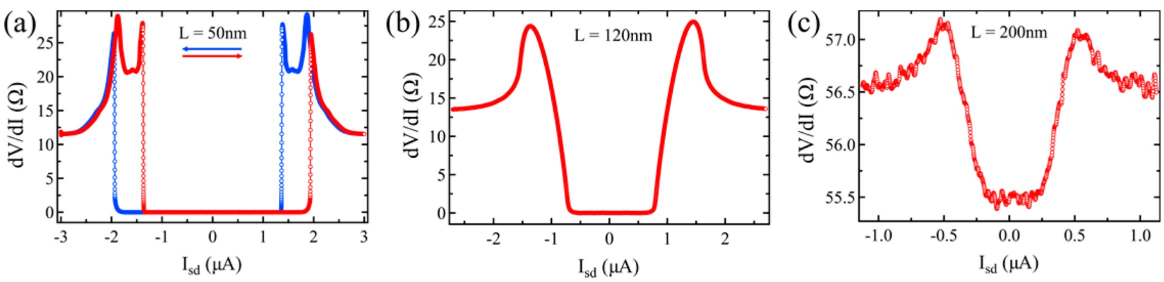

Figure 4. Current-biased dV/dI sweeps for different length of the weak links as a function of the bias current I_{sd}. (a) For a weak link with $L < L_\Phi$ pronouced peaks in the differential resistance at the flanks of the induced superconducting gaps ($dV/dI = 0\ \Omega$) are observed. The red and blue arrows indicate the sweep direction of the current. (b) For $L \approx L_\Phi$, the superconductivity is still fully gapped, but no flanking peaks occur, and the superconducting gap is not sharp. (c) For $L > L_\Phi$, the proximity superconductivity does not cover the entire weak link, and the junctions remains resistive.

measurements at 2 K (not presented) shows that the charge-carrier type is strongly hole-like and the carrier density is about $n \approx 4.5 \times 10^{20}$ cm^{-3}. Because SnTe is known to tend intrinsically to high carrier concentrations due to Sn vacancies (and, hence, to p-type behavior), this is consistent with current reports of other researchers.[19] An established all-electrical method of testing the presence of surface state transport are measurements of the longitudinal magnetoresistance (MR), in which a weak anti-localization (WAL) is expected due to surface states.[20] The MR data shown in Figure 3a are plotted as relative change in magneto-conductivity (MC) $\Delta\sigma_{2D} = \sigma(B) - \sigma(0)$ and show sharp cusp-like MR, which can indeed be attributed to WAL and evaluated with the Hikami-Larkin-Nagaoka (HLN) formalism:

$$\Delta\sigma_{2D} = \alpha\frac{e^2}{2\pi^2\hbar}\left(\ln\left(\frac{\hbar}{4eBL_\phi^2}\right) - \psi\left(\frac{1}{2} + \frac{\hbar}{4eBL_\phi^2}\right)\right) \tag{2}$$

where e is the electron charge, $\hbar$ is the Planck's constant, L_Φ is the phase-coherence length of a charge carrier in a given surface channel, $\psi(x)$ is the digamma function, B is the out-of-plane applied magnetic field, and α_0 is a dimensionless transport parameter.[20,21] Data fitting yields information about L_Φ and α_0, which are both plotted as a function of temperature T in Figure 3b. L_Φ is increasing steadily with decreasing T from $L_\Phi \approx 20$ nm at 20 K to $L_\Phi \approx 120$ nm at 2 K, which is the same order of magnitude as stated for other topological materials.[21−23] The coherence length, we obtained from the WAL data is much larger than the mean grain size of the bulk SnTe. Thus, it is well justified to attribute the value of 120 nm to the surface conduction channels. The theoretical prediction of the latter is supposed to yield $\alpha_0 = -0.5$ for one TSS contributing to transport.[20] As shown in Figure 3b, the fit of our data results in $\alpha \approx -0.5$ over the entire temperature range demonstrating topological protected transport. A total of four TSS exist on the surface Brillouin zone (SBZ) of a TCI, each entering with an additional $\alpha_0 = -0.5$ contribution. If one considers that TSS occur at the top and bottom interface, one would end up with a sum of $|\alpha| = 4$.[24] A plausible explanation of one single TSS per surface is most likely due to the valley degeneracy of the SnTe SBZ, giving rise to two different coupling scenarios: intra- and intersurface valley coupling. The first effect can be observed when a carrier is able to scatter coherently between Dirac valleys located on the same surface. Accordingly, a long coherence length results in strong intravalley coupling and, thus, a smaller α; similar behavior is typically observed for other 2D Dirac valley materials such as graphene.[25] The second scatter mechanism is intersurface valley coupling between top and bottom surface valleys. In this coupling regime, charge carriers can scatter coherently between the top and bottom SBZ Dirac valleys via bulk. This scenario has been observed by several other groups[24,26,27] and was attributed to the high bulk carrier concentration. Because WAL, however, is predominantly a 2D phenomenon, the bulk bands are unlikely to be the origin of the WAL.[21,24,28] While WAL has been observed as well in Rashba-split semiconductors,[29−31] such an explanation is ruled out here due to the high carrier concentration of our films.[26] Thus, the WAL features seen in Figure 3a can be considered as consequence of spin-momentum locking of the TCI TSS, but the bulk bands have strong influence on the WAL due to coupling to TSS transport channels.

SnTe/Nb SQUID Proximity-Induced Superconductivity. In the Figure 4a−c, results of the differential resistance (dV/dI) as

DOI: 10.1021/acs.nanolett.7b04870
Nano Lett. 2018, 18, 1264−1268

a function of the bias current I_{sd} for Josephson junction lengths (L_J) of 50, 120, and 200 nm are presented, respectively. If not further stated, all measurements are taken at 85 mK. The lengths of the weak links cover the range of the phase-coherence length L_Φ of the surface state electrons evaluated from the WAL data by HLN analysis. Hence, if surface state properties are contributing to the transport, the features resulting from proximity of the TSS to the Nb should be most prominent for L_J = 50 nm in the dV/dI data (Figure 4a). The individual sweeps can be separated into two sections: first, when I_{sd} is lower than the critical current I_c = 1.89 μA, a dissipationless supercurrent can flow through the system, and the device exhibits a clear zero-resistant state. No spectroscopic features are observed in the gap, so that we can exclude, e.g., quasiparticle hybridization effects, which are known to appear in topological materials. Second, for a bias current larger than I_c, the SQUID can be characterized by its normal state resistance $R_n \approx 12\ \Omega$. Small hysteretic behavior of the switching between both regions is present. While sweeping back (forth) from high positive (negative) bias currents, one can identify small retrapping currents of I_R = 1.39 μA. A plausible explanation for the hysteretic behavior are self-heating effects.[32] The most-prominent features in this dV/dI data are the strong peaks appearing at the outer-gap sides while sweeping forth (back) from the resistive state into the superconducting gap at $I = \pm$ 1.91 μA. Interestingly, when sweeping forth (back) from the inner nonresistive gap-region, the system jumps at the same current back into the resistive state, where the back (forth) biased current reveals the most prominent peak. We attribute the peaks to the contribution of the TSS carrying supercurrents. In this picture, surface Andreev bound states (SABS) generated in analogy to the mirror-protected Dirac points on the (001) surface of the SnTe crystal can host Cooper pairs, which are more robust and manifest themselves as additional peaks outside the bulk-superconducting gap. Hashimoto et al.[33] predicted such mirror-protected SABS hosted in superconducting TCI on the (001) surface if an odd-parity potential is realized. In Figure 4b, the length of the weak link corresponds to the estimated coherence length of the surface channels (L_J = 120 nm $\approx L_\Phi$), and hence, features due to SABS are expected to be weakened but still be present. The induced superconductivity still shows a zero-resistive behavior in the gap, but the observed gap-flanking SABS peaks vanished. Interestingly, the superconducting gap flanks are not showing a sharp jump as in Figure 4a but appear to be tilted outward, which suggests that pure s-wave type is unlikely. If superconductivity is partially carried by TSS, it is theoretically predicted that a mixture of s- and p-wave pairing is present.[34] In Figure 4c, the differential resistance sweeps of a device with a weak link of L_J = 200 nm ($>L_\Phi$) is shown. For this length, an induced superconducting gap is still observable, but it does no longer exhibit a zero-resistance state, keeping a finite in-gap resistance of $R \approx 55\ \Omega$. Results for other samples suggest that a zero resistance states exists for L_J < 175 nm. This result supports the suggestion that the phase-coherence length of the surface currents and the coherence length of the Cooper pairs are correlated and have crucial influence on the proximity-induced superconductivity in our films.

SnTe/Nb SQUID Oscillations. The response of the differential resistance dV/dI to an out-of-plane magnetic field B_z reveals clear oscillations in I_c shown in the color-code plot in Figure 5 for a length L_J = 120 nm and a field range from 0 to 1.1 mT (note that the oscillations persist up to B_z > 10 mT).

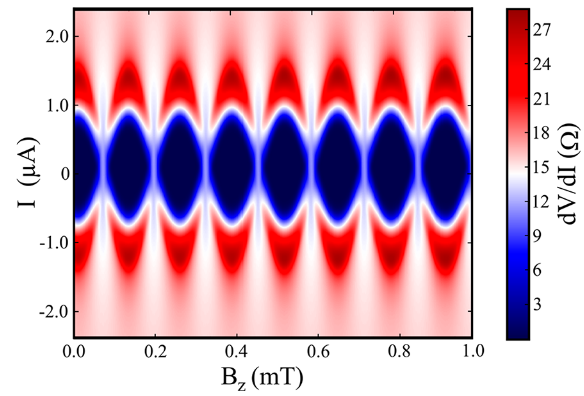

Figure 5. dV/dI color-plot showing the SQUID response (dV/dI as a function of B_z and I) to an external out-of-plane magnetic field B_z and bias current I. Clear oscillations are observable. The critical current I_c oscillates with the period δ_B = 122 μT that corresponds to an effective SQUID area of A_S = 16.9 μm^2, obeying the conventional ϕ_0-relation. The measurement has been offset to $I_c(0)$ = max.

The blue regions correspond to a SQUID resistance R = 0 Ω, while white and red areas represent finite resistance states. This mapping allows the evaluation of the critical current response for each value of the magnetic field B_z. The oscillations are periodic for δ_B = 122 μT. If one takes a closer look at eq 1, this corresponds to an effective area of A_S = 16.9 μm^2, which is in reasonable agreement with the dimensions of the SQUID rings characterized in our experiment if one considers the London penetration length of Nb λ_{Nb} = 350 nm[35] on all sides of the square. Thus, we conclude that the data shows only conventional critical current response through the surface supercurrents, and hence, no 4π-periodic modulation is observed. Our finding agrees with the results of similar experiments performed by other groups on other topological materials, such as strained HgTe or Bi_2Te_3 and Bi_2Se_3 compounds.[35−37] The reason for the absence of 4π-periodicity may be a 2π-signal poisoning arising from the dominating amounts of supercurrents carried by bulk channels, which dominate the transport. This 2π channels coexist with a contribution of $k_y \neq 0$ (k_y is the wave vector-component transversal to the moving direction k_x). Under these circumstances the predicted zero-energy Andreev bound excitations (Majorana Fermions) are gapped out.[38] The small influence of the unique 4π-periodic topological modes would than elusively vanish within this parasitic background. Here, we emphasize that doping-dependent and (locally) gated measurements,[39] as well as RF-transport analysis[40] are necessary next steps to address this problem and access the new field of Majorana physics in TCI thin film systems.

Conclusions. In conclusion, we have demonstrated WAL in the TCI SnTe and the first experimental evidence of fully gapped superconductivity in SnTe/Nb heterostructures at T = 85 mK and a length of Josephson junction weak links below L_J < 175 nm. The phase-coherence length of the TCI extracted from these two properties show reasonable agreement. We additionally investigated the response of Nb-SQUIDs patterned on top of the SnTe to a perpendicular magnetic field. The measured SQUID oscillations follow the relation describing a conventional SQUID interference pattern. Here, our results form a foundation for future investigations of proximity-induced topological superconductivity in the class of topological crystalline matter.

DOI: 10.1021/acs.nanolett.7b04870
Nano Lett. 2018, 18, 1264−1268

■ ASSOCIATED CONTENT

Supporting Information

The Supporting Information is available free of charge on the ACS Publications website at DOI: 10.1021/acs.nanolett.7b04870.

A detailed description of the SnTe thin films growth and film characterization with XRD, AFM, TEM, and texture measurements. (PDF)

■ AUTHOR INFORMATION

Corresponding Authors

*E-mail: rklett@physik.uni-bielefeld.de.
*E-mail: reiss@physik.uni-bielefeld.de.

ORCID

Robin Klett: 0000-0002-6348-495X

Notes

The authors declare no competing financial interest.

■ ACKNOWLEDGMENTS

The financial support by the Deutsche Forschungsgemeinschaft (DFG, German Research Foundation) within the priority program SPP 1666 "Topological Insulators" is gratefully acknowledged.

■ REFERENCES

(1) Ando, Y.; Fu, L. *Annu. Rev. Condens. Matter Phys.* **2015**, *6*, 361–381.
(2) Hsieh, T.; Lin, H.; Liu, J.; Duan, W.; Bansil, A.; Fu, L. *Nat. Commun.* **2012**, *3*, 982.
(3) Tanaka, Y.; Ren, Z.; Sato, T.; Nakayama, K.; Souma, S.; Takahashi, T.; Segawa, K.; Ando, Y. *Nat. Phys.* **2012**, *8*, 800–803.
(4) Tanaka, Y.; Shoman, T.; Nakayama, K.; Souma, S.; Sato, T.; Takahashi, T.; Novak, M.; Segawa, K.; Ando, Y. *Phys. Rev. B: Condens. Matter Mater. Phys.* **2013**, *88*, 235126.
(5) Okada, Y.; Serbyn, M.; Lin, H.; Walkup, D.; Zhou, W.; Dhital, C.; Neupane, M.; Xu, S.; Wang, Y. J.; Sankar, R.; Chou, F.; Bansil, A.; Hasan, M. Z.; Wilson, S. D.; Fu, L.; Madhavan, V. *Science* **2013**, *341* (6153), 1496–1499.
(6) Sessi, P.; Di Sante, D.; Szczerbakow, A.; Glott, F.; Wilfert, S.; Schmidt, H.; Bathon, T.; Dziawa, P.; Greiter, M.; Neupert, T.; Sangiovanni, G.; Story, T.; Thomale, R.; Bode, M. *Science* **2016**, *354* (6317), 1269–1273.
(7) Zhang, F.; Kane, C. L.; Mele, E. J. *Phys. Rev. Lett.* **2013**, *111*, 056403.
(8) Shiozaki, K.; Sato, M. *Phys. Rev. B: Condens. Matter Mater. Phys.* **2014**, *90*, 165114.
(9) Sasaki, S.; Ando, Y. *Cryst. Growth Des.* **2015**, *15* (6), 2748–2752.
(10) Balakrishnan, G.; Bawden, L.; Cavendish, S.; Lees, M. R. *Phys. Rev. B: Condens. Matter Mater. Phys.* **2013**, *87*, 140507.
(11) Sato, T.; Tanaka, Y.; Nakayama, K.; Souma, S.; Takahashi, T.; Sasaki, S.; Ren, Z.; Taskin, A. A.; Segawa, K.; Ando, Y. *Phys. Rev. Lett.* **2013**, *110*, 206804.
(12) Stanescu, T. D.; Sau, J. D.; Lutchyn, R. M.; Das Sarma, S. *Phys. Rev. B: Condens. Matter Mater. Phys.* **2010**, *81* (24), 094522.
(13) Chung, S. B.; Horowitz, J.; Qi, X. *Phys. Rev. B: Condens. Matter Mater. Phys.* **2013**, *88*, 214514.
(14) Tung, Y. W.; Cohen, M. L. *Phys. Rev. B* **1970**, *2*, 1216.
(15) Blonder, G. E.; Tinkham, M.; Klapwijk, T. M. *Phys. Rev. B: Condens. Matter Mater. Phys.* **1982**, *25* (7), 4515–4532.
(16) Strijkers, G. J.; Ji, Y.; Yang, F. Y.; Chien, C. L.; Byers, J. M. *Phys. Rev. B: Condens. Matter Mater. Phys.* **2001**, *63*, 104510.
(17) Zeljkovic, I.; Walkup, D.; Assaf, B. A.; Scipioni, K. L.; Sankar, R.; Chou, F.; Madhavan, V. *Nat. Nanotechnol.* **2015**, *10* (10), 849–853.
(18) Yan, C.; Guo, H.; Wen, J.; Zhang, Z.; Wang, L.; He, K.; Ma, X.; Ji, S.; Chen, X.; Xue, Q. *Surf. Sci.* **2014**, *621*, 104–108.
(19) Mengui, U. A.; Abramof, E.; Rappl, P. H. O.; Ueta, A. Y. *Braz. J. Phys.* **2006**, *36* (2A), 324–327.
(20) Hikami, S.; Larkin, A. I.; Nagaoka, Y. *Prog. Theor. Phys.* **1980**, *63* (2), 707–710.
(21) He, H. H.; Wang, G.; Zhang, T.; Sou, I.-K.; Wong, G. K. L.; Wang, J.-N.; Lu, H.-Z.; Shen, S. Q.; Zhang, F.-C. *Phys. Rev. Lett.* **2011**, *106* (16), 166805.
(22) Shekhar, C.; Kampert, E.; Foerster, T.; Yan, B.; Nayak, A.; Nicklas, M.; Felser, C. Large linear magnetoresistance and weak anti-localization in Y(Lu)PtBi topological insulators. 2015, *arXiv:1502.00604*. arXiv.org e-Print archive. https://arxiv.org/abs/1502.00604 (accessed on November 14, 2017).
(23) Zhao, B.; Cheng, P.; Pan, H.; Zhang, S.; Wang, B.; Wang, G.; Xiu, F.; Song, F. *Sci. Rep.* **2016**, *6*, 22377.
(24) Akiyama, R.; Fujisawa, K.; Yamaguchi, T.; Ishikawa, R.; Kuroda, S. *Nano Res.* **2016**, *9* (2), 490–498.
(25) Wu, X.; Li, X.; Song, Z.; Berger, C.; de Heer, W. A. *Phys. Rev. Lett.* **2007**, *98*, 136801.
(26) Assaf, B. A.; Katmis, F.; Wei, P.; Satpati, B.; Zhang, Z.; Bennett, S. P.; Harris, V. G.; Moodera, J. S.; Heiman, D. *Appl. Phys. Lett.* **2014**, *105*, 102108.
(27) Shen, J.; Xie, Y.; Cha, J. J. *Nano Lett.* **2015**, *15* (6), 3827–3832.
(28) Bao, L.; He, L.; Meyer, N.; Kou, X.; Zhang, P.; Chen, Z.; Fedorov, A.; Zou, J.; Riedemann, T. M.; Lograsso, T. A.; Wang, K. L.; Tuttle, G.; Xiu, F. *Sci. Rep.* **2012**, *2*, 726.
(29) Bergmann, G. *Phys. Rep.* **1984**, *107*, 1.
(30) Kallaher, R. L.; Heremans, J. J. *Phys. Rev. B: Condens. Matter Mater. Phys.* **2009**, *79*, 075322.
(31) Roulleau, P.; Choi, T.; Riedi, S.; Heinzel, T.; Shorubalko, I.; Ihn, T.; Ensslin, K. *Phys. Rev. B: Condens. Matter Mater. Phys.* **2010**, *81*, 155449.
(32) Courtois, H.; Meschke, M.; Peltonen, J. T.; Pekola, J. P. *Phys. Rev. Lett.* **2008**, *101*, 067002.
(33) Hashimoto, T.; Yada, K.; Sato, M.; Tanaka, Y. *Phys. Rev. B: Condens. Matter Mater. Phys.* **2015**, *92*, 174527.
(34) Fu, L.; Kane, C. L. *Phys. Rev. Lett.* **2008**, *100*, 096407.
(35) Maier, L.; Bocquillon, E.; Grimm, M.; Oostinga, J. B.; Ames, C.; Gould, C.; Brüne, C.; Buhmann, H.; Molenkamp, L. W. *Phys. Scr.* **2015**, *T164*, 014002.
(36) Veldhorst, M.; Molenaar, C. G.; Wang, X. L.; Hilgenkamp, H.; Brinkman, A. *Appl. Phys. Lett.* **2012**, *100*, 072602.
(37) Kurter, C.; Finck, A. D. K.; Hor, Y. S.; Van Harlingen, D. J. *Nat. Commun.* **2015**, *6*, 7130.
(38) Oostinga, J. B.; Maier, L.; Schüffelgen, P.; Knott, D.; Ames, C.; Brüne, C.; Tkachov, G.; Buhmann, H.; Molenkamp, L. W. *Phys. Rev. X* **2013**, *3*, 021007.
(39) Bocquillon, E.; Deacon, R. S.; Wiedenmann, J.; Leubner, P. L.; Klapwijk, T. M.; Brüne, C.; Ishibashi, K.; Buhmann, H.; Molenkamp, L. W. *Nat. Nanotechnol.* **2016**, *12*, 137–143.
(40) Wiedenmann, J.; Bocquillon, E.; Deacon, R. S.; Hartinger, S.; Herrmann, O.; Klapwijk, T. W.; Maier, L.; Ames, C.; Brüne, C.; Gould, C.; Oiwa, A.; Tarucha, S.; Buhmann, H.; Molenkamp, L. W.; Ishibashi, K. *Nat. Commun.* **2016**, *7*, 10303.

DOI: 10.1021/acs.nanolett.7b04870
Nano Lett. 2018, 18, 1264–1268